Active vibration control of a cable-driven parallel robot using active rods

Florian Lacaze, Romain Delpoux, Didier Remond, Simon Chesne

Mechanics & Industry **25**, 27 (2024)
© F. Lacaze et al., Published by EDP Sciences 2024
https://doi.org/10.1051/meca/2024024

Mechanics & Industry

Available online at:
www.mechanics-industry.org

REGULAR ARTICLE OPEN ACCESS

Active vibration control of a cable-driven parallel robot using active rods

Florian Lacaze[1], Romain Delpoux[2], Didier Remond[1], and Simon Chesne[1,*]

[1] INSA Lyon, CNRS, LaMCoS, UMR5259, 69621 Villeurbanne, France
[2] Univ Lyon, INSA-Lyon, CNRS UMR5005, Laboratoire Ampère, 69621, France

Received: 31 October 2023 / Accepted: 4 September 2024

Abstract. This study deals with the integration of two active rods on a cable-driven parallel robot (CDPR) to control its vibrations. Three control laws derived from Integral Force Feedback (IFF) are proposed and compared analytically using a dynamic CDPR model: $\alpha\beta$-IFF, IFF with filters and IFF with positive proportional feedback (PIFF). A prototype was set up to test the performance of the active rods. A parametric study was then carried out on this prototype to choose the best control law and optimise its parameters. The use of only two active rods over eight driven cables allowed reducing the vibration levels over the six modes of the robot.

Keywords: Cable-driven parallel robot / vibration control / active rods / integral force feedback / piezoelectric transducers

1 Introduction

A Cable-Driven Parallel Robot (CDPR) is a type of parallel kinematic manipulator in which cables link a mobile platform called an effector to a fixed base. The effector moves due to the controls performed by motors on the lengths and tensions of the cables. The development of CDPRs in industry has been studied for a wide range of applications due to their low cost and adaptability, for example for object visualisation [1,2], haptic perception [3], and handling heavy materials [4]. CDPRs have also recently been considered for printing large 3D objects [5]. Furthermore, compared to a rigid body transmission, the use of cables enables reducing the inertia of the mobile part; CPDRs can also reach high accelerations and be used for high speed manipulation [6]. However, the lack of rigidity and the low internal damping of a CDPR raises issues such as lack of accuracy, the occurrence of vibrations, and noise propagation.

To overcome these problems, several solutions have been studied. The stiffness of the fully-constrained CDPR FALCON was increased by creating internal forces [7]. In [8,9], input shaping methods were used to eliminate vibrations on the CDPR. Input shaping methods are based on the convolution of a sequence of pulses with an arbitrary command. The pulse frequencies and amplitudes are obtained from the frequencies and damping rates of the modal space. In [10], a fuzzy controller was designed to reduce the wind-induced vibrations. Another way to control the vibrations of a CDPR is to add active devices. An internal wrench can be generated by adding reaction wheels on the effector [11] and simulations showed in [12] that an active stabilizer consisting of actuated rotating arms installed on-board the CDPR effector can reduce vibrations. Moreover, it is theoretically possible to stabilize planar cable-driven systems in non-planar directions using cables alone [13,14]. To reduce vibrations and increase damping in similar systems, such as cable structures [15], cable-stayed bridges [16,17] or cable actuated systems [18], the integration of active mounts composed of piezoelectric sensors, actuators and control units has been proposed. Piezoelectric transducers have proven their efficiency for cable structures. In [19], decentralized integral force feedback (IFF) was proposed to enhance the dynamic stability of a thin aperture light collector (TALC). Using the IFF controller, the actuator is driven with a signal proportional to the integral of the sensor force. Preumont et al. [20,21] demonstrated that the open-loop transfer function has alternating poles and zeros and that the system is unconditionally stable if the actuator and the sensor are collocated, and if the hysteresis or the time delay of the actuator is negligible. IFF is well-known to be a relatively simple solution because it does not require prior knowledge of the system controlled. However, one of the main limitations of the IFF is the degradation of compliance at low frequencies, compromising the capacity of disturbance elimination. Moreover, in practice, the signal measured by the sensor has a non-zero mean, so the integral increases over time and goes beyond the limits of

* e-mail: simon.chesne@insa-lyon.fr

the actuator. Another problem is high frequency electrical noise, which causes instabilities. It has been shown that a compromise can be achieved by applying adequately high-pass and low-pass filtering to the control signal [21,22]. Chesne et al. [23] proposed a modification of the IFF to overcome these drawbacks through the $\alpha\beta$-IFF control. They demonstrated that the addition of a pair of poles and a zero can significantly increase the active damping of a selected mode.

This paper presents a new approach to reduce vibrations on a CDPR generated by the displacement of the effector. Two cables are equipped with two active rods, using piezoelectric transducers which reduce vibrations by actively increasing the damping. In this kind of CDPR, because of the stiffness of the structure, the force generated by a piezoelectric actuator is the product of the stiffness and the displacement, and it is adequate to counteract the structure's vibrations. Another novelty is that the active tendons are embedded next to the effector and are therefore in motion, which adds complexity to the active control. To this end, two controllers will be used for the active rods: a classical IFF controller with filters and an $\alpha\beta$-IFF controller. The authors also propose to add a positive proportional feedback that slightly improves the damping of the control law [24]. The paper is structured as follows: Section 2 introduces the CDPR and a simple dynamic model. The controllers used for active control are introduced in Section 3 and an estimation of the performance of the control device is performed. Section 4 presents the experimental set-up used in the study. Section 5 investigates the parametric optimisation and the experimental results. Finally, Section 6 draws the conclusions and discusses future works.

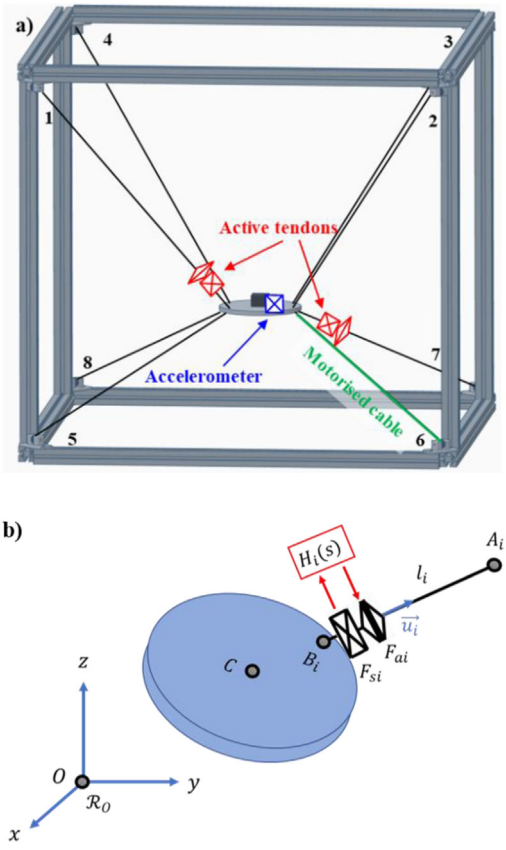

Fig. 1. (a) The CDPR, with one motorised cable and two active rods; (b) diagram of the effector with one cable and the corresponding notations.

2 Presentation of the CDPR and its dynamic modelling

2.1 Presentation

In this paper, a CDPR with 8 cables is considered, as shown in Figure 1. The 8 pulley anchor points A_i are located in the corners of a 1 m square aluminium profile cube. Steel cables with a diameter of 0.54 mm are used. Each cable is tensioned with a 2 kg mass so that the resulting structure has natural frequencies suitable for the transducers and remains controllable by the motor used. The displacement is generated by a single electric motor located on the 6^{th} cable. This restricts the study to a movement along one axis, however this movement is sufficient to excite the system and characterise the performance of the vibration control. The cables are linked to an effector designed to have a higher stiffness [25]. It has a r_e =5.5 cm radius and is made of polylactic acid (PLA). A mass is added to this effector to increase its total weight (m_e = 782 g). The performance in terms of vibration is measured with a 3-axis accelerator installed on the effector. The first acceleration corresponds to a movement in the direction close to that of the motorised cable, the second to a vertical movement and the third to a movement transverse to the motorised movement. To control the vibrations, two active systems are mounted on cables 1 and 7. They are each composed of a piezoelectric force sensor and a piezoelectric actuator in series.

2.2 Dynamic modelling

In the Laplace domain, the displacements $\vec{X}$ of the effector are given by the cable tensions $\vec{T}$, and a perturbation force denoted $\vec{F}$ [26]:

$$M s^2 \vec{X}(s) = J_u \vec{T}(s) + \vec{F}(s). \tag{1}$$

The Jacobian matrix J_u maps of cable tension in forces and momentums on the platform:

$$J_u = \begin{bmatrix} \overrightarrow{u_1^0} & \dots & \overrightarrow{u_m^0} \\ \overrightarrow{CB_1^0} \wedge \overrightarrow{u_1^0} & \dots & \overrightarrow{CB_m^0} \wedge \overrightarrow{u_m^0} \end{bmatrix}_{6\times 8} \tag{2}$$

where $\overrightarrow{CB_i^0}$ is the vector between the effector centre C and the anchor point B_i, $\vec{u_i^0}$ is the unitary orientation vector of the i^{th} cable, i.e. $\overrightarrow{u_i^0} = \dfrac{\overrightarrow{B_i A_i^0}}{\left\| \overrightarrow{B_i A_i^0} \right\|}$. The mass matrix is

$$M = \begin{bmatrix} m_e * I_3 & O_3 \\ O_3 & I_e \end{bmatrix}_{6\times 6}, \text{ where}$$

$$I_e = \mathrm{m_e} * \mathrm{r_e^2} * \mathrm{diag}\left[\frac{1}{4}, \frac{1}{4}, \frac{1}{2}\right].$$

An active cable works by introducing a displacement Δ_i that changes the tension in the i^{th} active cable. This displacement will change the tension in the cable giving the equation:

$$\vec{T}_i(s) = -[k_i]\left(J_u^T \vec{X}(s) - \vec{\Delta}_i(s)\right) \tag{3}$$

where $[k_i]$ is a diagonal matrix containing the stiffnesses of the cables. For a central position, the stiffnesses are $k_i \simeq 2.0{*}10^4$ N/m. This value has been experimentally identified in [25]. Without control, the CDPR's modes can be obtained with the matrices $K = J_u[k_i]{J_u}^T$ and M; in the case of the home pose of the mobile platform, by solving the eigenvalue problem, their frequencies are 24.1 Hz, 31.5 Hz, 40.0 Hz, 41.2 Hz, 43.5 Hz and 65.1 Hz.

2.3 Modelling of active rods

The active displacement Δ_i depends on the characteristics of the actuator used, on the active signal F_{ai} and on the multiplicative constant C_a of the amplifier. A maximum displacement of $60{*}10^{-6}$ m over a voltage range of 160 V can be obtained with the two CEDRAT APA40SM actuators, thus $\Delta_i(s) = C_a \frac{F_{ai}(s)}{k_a}$, with $k_a = \frac{160}{60*10^{-6}} \simeq 2.6 * 10^6$ V/m and $C_a = 20$. F_{ai} is given directly by the control law H_i^j chosen (i designates the i^{th} cable and j denotes the control law chosen) and the tension F_{si} measured by the force sensor:

$$F_{ai}(s) = H_i^j(s) * F_{si}(s). \tag{4}$$

The conditioner of the piezoelectric force sensors acts as a high-pass filter at $\omega_c = 2\pi$ rad/s:

$$F_{si}(s) = \frac{s}{s+\omega_c} T_i(s). \tag{5}$$

Equation (6) is derived:

$$\Delta_i(s) = \frac{C_a}{k_a} H_i^j(s) \frac{s}{s+\omega_c} T_i(s). \tag{6}$$

The control laws proposed will be presented and detailed in the next section.

3 Active control and analytic discussion

3.1 Control laws

The simplest form of IFF is to drive the actuator with a signal $f_a\ (t)$ proportional to the integral of the force measured by the force sensor $f_s\ (t)$. Thus, the control force is given by $f_a(t) = g\int_0^t f_s(t)dt$, where g is the feedback gain. The control is decentralised and different gains g_i^0 can be used on each active cable. In the Laplace domain, the control laws can be written as: $H_i^0(s) = \frac{g_i}{s}$, with i designating the i^{th} cable.

In this contribution, two different control laws will be tested and the authors also suggest a modification of the first one to improve the resulting damping.

The first control law is a classical IFF with two first order filters. High-pass and low-pass filters are defined by their cut-off frequencies leading to equation (7):

$$H_i^1(s) = g_i^1 \frac{\omega_{LP}}{(s+\omega_{LP})(s+\omega_{HP})} \tag{7}$$

where ω_{LP} and ω_{HP} are respectively the cut-off frequencies of the low-pass and the high-pass filter. Unfortunately, with filtered IFF, the system's stability is no longer unconditional [21,22]. It is therefore possible to test a controller introduced by S. Chesne in [23] which guarantees stability, the $\alpha\beta$-IFF controller:

$$H_i^2(s) = g_i^2 \frac{s+\alpha}{(s+\beta)^2}. \tag{8}$$

For $|s| > \alpha$, the controller is essentially an integrator, as the classical IFF, and for $|s| < \alpha$, the controller is a double integrator, which tends to cancel the force applied by the effector, or to modify the stiffness, as the sensor force is partly proportional to the acceleration [24]. It has been shown that at low frequency this kind of controller present a loss of compliance, to recover it, S. Chesne proposed to also add a double real pole located at $s = -\beta$. This double real pole also plays the role of a double filter, and with this control law the low-pass and high-pass filters are no longer required.

In addition, a modification of the IFF controller is proposed in [24] to increase the damping of the modes by adding a positive proportional feedback term. The term "positive", even if the sign of p_i is negative in equation (11), is due to the fact that this correction is applied in a global negative feedback loop. The authors decided to apply this modification only to the filtered IFF to obtain a new control law named "Proportional and Integral Force Feedback" (PIFF) and given by:

$$H_i^3(s) = g_i^1 \frac{\omega_{LP}}{(s+\omega_{LP})(s+\omega_{HP})} - p_i. \tag{9}$$

In theory this controller is stable for $p < 1$, but the gain margin limits the value which can be used [24]. In practice in this case, instabilities appear from $p > 0.4$.

3.2 Analysis of the control laws

The analysis of the behaviour of the control laws is obtained using the dynamic modelling of the CDPR and the active tendons. For the sake of clarity, each control law is written as $H_i^j(s) = \frac{N_i^j(s)}{D_i^j(s)}$ with N_i^j being the numerator and D_i^j the denominator. Inserting equation (6) into equation (3) gives:

$$\vec{T}_i(s) = -[k_i * A_i(s)] * J_u^T \vec{X}(s) \tag{10}$$

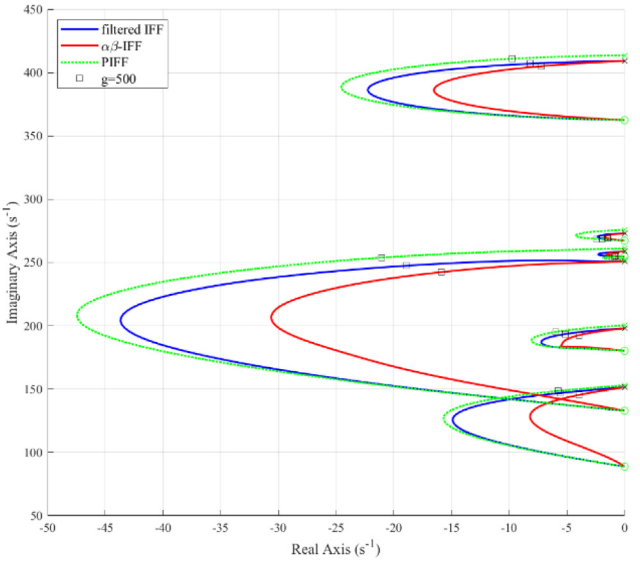

Fig. 2. Root locus with filtered IFF (blue), with $\alpha\beta$-IFF (red) and with PIFF (green).

where $A_i^j(s) = \frac{k_a D_i^j(s)(s+\omega_c)}{C_a k_i N_i^j(s) s - k_a D_i^j(s)(s+\omega_c)}$ and $\left[k_i * A_i^j(s)\right]$ is a diagonal matrix containing the $k_i * A_i^j(s)$. Equation (11) is derived from the dynamic equation (1).

$$s^2 M\vec{X}(s) + J_u[k_i * A_i(s)]J_u^T\vec{X}(s) = \vec{F}(s) \qquad (11)$$

Without control, the matrix $[A_i\ (s)]$ is an (8×8) identity matrix and the classical stiffness matrix $K = J_u\ [k_i]\ J_u T$ is obtained.

One can write $R(s) = s^2 M + J_u[k_i * A_i(s)]J_u^T$, then equation $\vec{X}(s) = R^{-1}(s)\vec{F}(s)$ allows plotting the root locus of the system, by solving $1/R_{ij}^{-1}(s) = 0$, for the same gains $g = g_1^j = g_7^j$. As the problem is MIMO and as there are several parameters for each control law, this section focuses only on the variation of gain g. Section 5 will focus on the experimental optimisation of the parameters and gains. To plot the different root locus in Figure 2 (filtered IFF in blue, $\alpha\beta$-IFF in red and PIFF in green), the values of parameters ω_{LP}, ω_{HP}, p_1, p_7, α and β obtained experimentally are used. In this model, six poles with strictly positive imaginary parts are depicted.

First, it can be seen that the system is stable for the three controllers and for any positive gain. It can also be seen that damping for the six modes is added by the use of two cables, but the control and damping rate vary according to the mode considered. Moreover, the configuration of the active rods will modify the performance according to the modes. It can be pointed out that the 3rd mode is the easiest to damp, i.e. that at 40 Hz. The root locus shows that the damping is higher with filtered IFF than with $\alpha\beta$-IFF on all modes. With the PIFF controller, the damping is slightly better for all modes. The squares on curves correspond to a gain $g = 500$, which is in the order of magnitude of the gain values in the experimental part. It shows that the controllability of the modes is slightly different. It can be observed that for this gain value the maximum damping is not reached and a larger gain could be required. Nevertheless, such a gain value cannot be reached during the experiment.

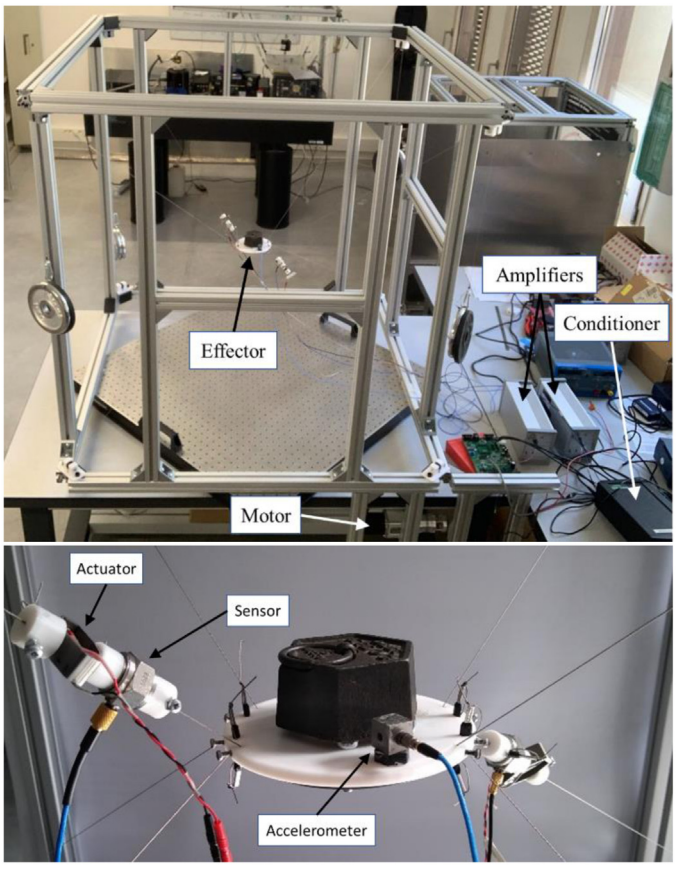

Fig. 3. The experimental set-up with the CDPR and a zoom on the effector.

4 Experimental set-up

The CDPR described in Section 2 is considered in the experimental set-up, as shown in Figure 3. In this contribution, the vibratory excitation is achieved by the movement of the effector, driven by the motor which moves backwards and forwards.

4.1 Motor control

For this application, motor control should not be overlooked. Indeed, poor motor control would generate unwanted vibrations. Our choice naturally turned to the Permanent Magnet Synchronous Machine (PMSM) using Field Oriented Control (FOC) Strategy. PMSMs are more suitable than DC motors or induction motors, since their overall weight and volume are significantly reduced for a given output power and provide better efficiency [27]. While the six step control is very easy to implement for this motor, FOC has the advantage of controlling the motor

currents and thus offers better management of the motor torque produced. This significantly reduces torque ripple on the motor shaft. Thanks to the use of Park transformation [28] the torque produced is directly proportional to the quadrature current i_q. The Park transformation and current controller are implemented using the SSpace 1104 rapid control prototyping system.

4.2 Active rods

To control vibrations generated by the effector movements, 2 active systems are mounted on cables 1 and 7. They are each composed of a piezoelectric force sensor and a piezoelectric actuator. These active rods have the particularity of being embedded and moving when the platform moves, unlike those used in cable-stayed bridges [16,17] and in the TALC [19]. In addition, one conditioner is used for the sensors and two load amplifiers are used for the actuators. Classical DSpace DS1104 controller board is used for the real-time measurement and control of the motor and the actuators, making it easy to implement the control laws introduced earlier.

5 Parametric optimization and experimental results

5.1 Vibratory excitation

The vibratory excitation is achieved by the movement of the effector driven by the motor. It moves backwards and forwards according to step5 functions, described in equation (12), which avoids shocks and discontinuities. The Step5 function is a step from $\theta_1 = \theta\ (t_1)$ to $\theta_2 = \theta\ (t_2)$ smoothed by a 5^{th} degree polynomial; this means that the velocities at t_1 and t_2 are both equal to zero.

$$\theta(t) = steps5(t) = \begin{cases} \theta_1 & if\ t < t_1 \\ \theta_1 + (\theta_2 - \theta_1)\ \Delta\ (t)^3 & \\ *\left(10 - 15\ \Delta\ (t) + 6\ \Delta\ (t)^2\right) & if\ t_1 < t < t_2 \\ \theta_2 & if\ t \geq t_2 \end{cases} \quad (12)$$

with $\Delta(t) = \frac{t - t_1}{t_2 - t_1}$.

Figure 4 represents an illustration of the resulting displacement. In this paper, these parameters are set to $t_2 - t_1$=0.5 s and the steps are between − 0.3 and 0.3 rad every 1 s, which means that there is a 0.5 s pause after each movement.

5.2 Parametric optimization

A parametric optimization is performed on the filtered IFF controller and on the $\alpha\beta$-IFF. Each control law has two gains (g_1^j and g_7^j) and two additional parameters ($\omega_{LP}\ \omega_{HP}$ for the filtered IFF, and $\alpha\ \beta$ for $\alpha\beta$ −IFF). It was decided to start by optimising the additional parameters and then the gains. Indeed, the values of the additional parameters modify the signal magnitude before multiplying by the gains, thus they have an impact on the optimal gains. For each combination of two parameters, the platform is moved 15 times forwards and backwards in 30 s.

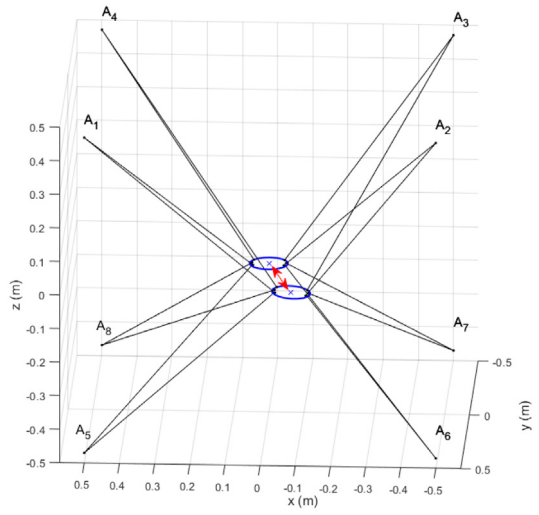

Fig. 4. Illustration of the displacement for the angular rotation of the motor.

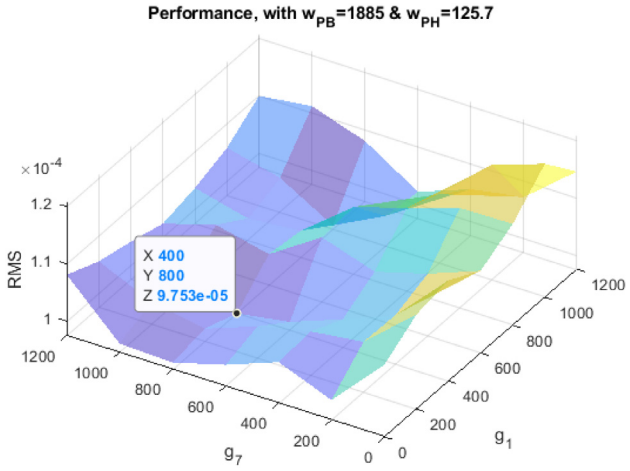

Fig. 5. RMS value versus parameters g_1 and g_7.

For the quantity to be optimised, the authors chose to use the root of the area under the Power Spectral Density (PSD) curve of the first acceleration: the vibration levels are therefore expressed in V^2/Hz, a unit homogeneous to a power describing the energy injected by the vibrations at a given frequency. The root of the area under the PSD curve therefore corresponds to the root mean square (RMS) value. PSD is obtained using Welch's method [29].

The first optimisation is dedicated to the low-pass and high-pass filter frequencies, and the lowest RMS value is reached for $\omega_{LP} = 2\pi$*300 rad/s and $\omega_{HP} = 2\pi$*20 rad/s. In the second step the gains of the two controllers are optimized and their values are derived:$g_1^1 = 400$ and $g_7^1 = 800$. An example of the evolution of the RMS value versus the gains is given in Figure 5. It can be seen that the

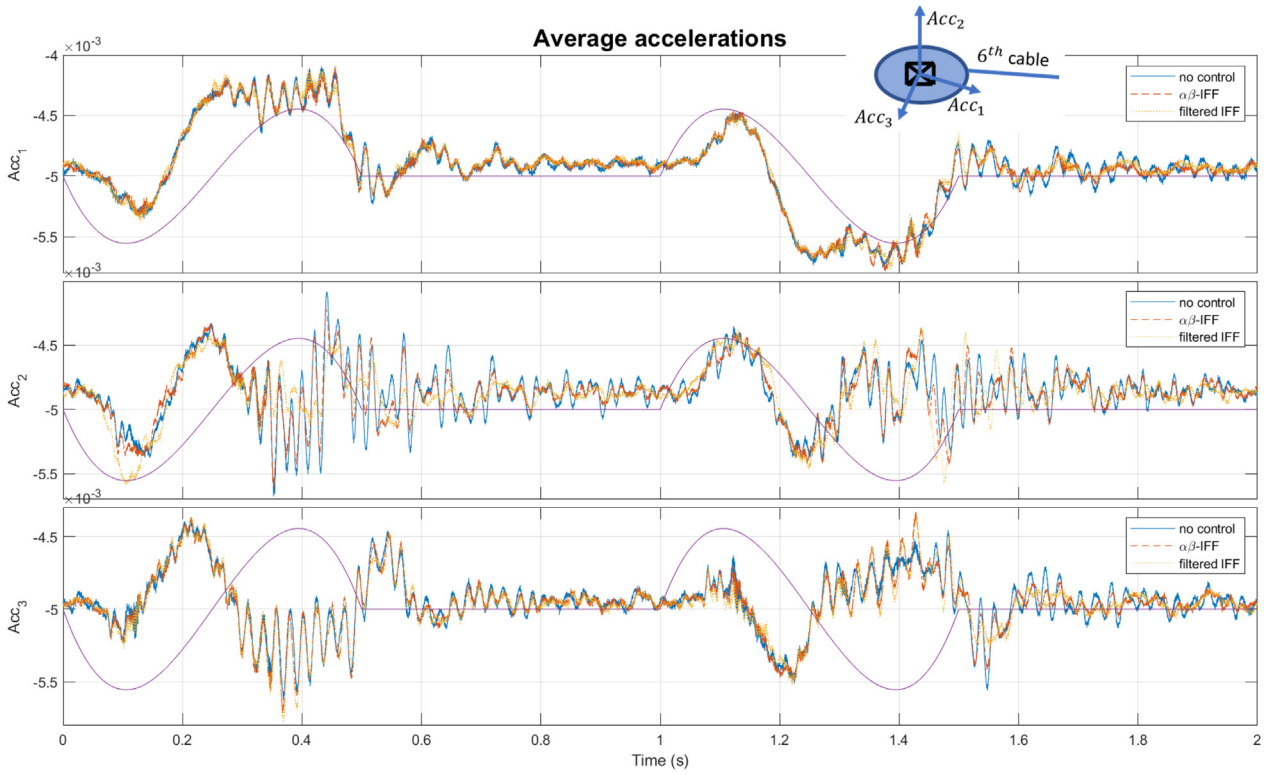

Fig. 6. Average of the acceleration signals without control (blue), with $\alpha\beta$-IFF (red) and with filtered IFF (yellow).

functional is not smooth, which exhibits that the dynamics of the system is complex and clearly non-linear. The same experiment is repeated with the $\alpha\beta$ −IFF controller, and the optimization provides the following values: $\alpha = 10$ and $\beta = 80$, $g_1^2 = 200$ and $g_7^2 = 600$. For the PIFF control, the optimal parameters of the filtered IFF are kept and the same parametric optimisation is used to tune the gains of the proportional feedback. It gives $p_1 = 0.2$ and $p_7 = 0.075$. These values will be used in the next section to illustrate the performance of the control device.

5.3 Experimental results

The control laws introduced in Section 3 were then compared experimentally. The previous experiment was replicated for 300 s with the parameters obtained by optimisation for each control law: without control, with IFF with low-pass and high-pass filters, with $\alpha\beta$-IFF and with PIFF controllers. The acceleration signals were averaged over 2 s, which corresponds to one step forwards and one step backwards. Figure 6 shows the signals obtained. The purple curve represents an image of the angular acceleration of the motor consisting of *step5* functions. The shape of the measured acceleration naturally depends on the excitation of the motor. Thanks to active control, there was a decrease in vibration in the time domain acceleration signal, especially visible on the first part of the first and second acceleration signals, and on the second part for the third acceleration. These results are related to the configuration of the active rods and good performance on acceleration 3 is explained by the fact that the orientations of cables 1 and 7 mainly follow a direction similar to the third measured acceleration.

To better distinguish the benefits on the different modes, the PSD of the acceleration signals are plotted in Figure 7. The PSD shows very good performance in the 3 main modes observed for the 3 directions. Also, the result is better with the filtered IFF controller, which is consistent with the root locus obtained in Figure 2.

Table 1 summarises the frequencies of the main modes and the improvements for each mode compared to no control. The frequencies obtained are close to those obtained with the model in Section 2 (24.1 Hz, 31.5 Hz, 40.0 Hz, 41.2 Hz, 43.5 Hz, 65.1 Hz). The difference can be explained by the use of a simple model: the cables are only elastic, the inertia matrix of the effector is only estimated, the inertia of the sensors and actuators are not considered in the model, nor is the preload of the cables. The results are better for accelerations 1 and 3, which correspond to non-vertical movements, and for the 36 Hz mode. An analogy with the root locus which predicted better damping for this mode can be noted.

Figure 8 gives an example of PSD obtained without control, and with the filtered IFF and PIFF controllers. The improvement achieved is low with PIFF. The benefit obtained is more visible in Table 2 which shows that the PIFF controller reduces the level of vibration in all directions. Although the parametric optimisation was performed on acceleration 1, the performance are also good for accelerations in other directions and show that the proposed control laws and the parametric optimisation are quite robust.

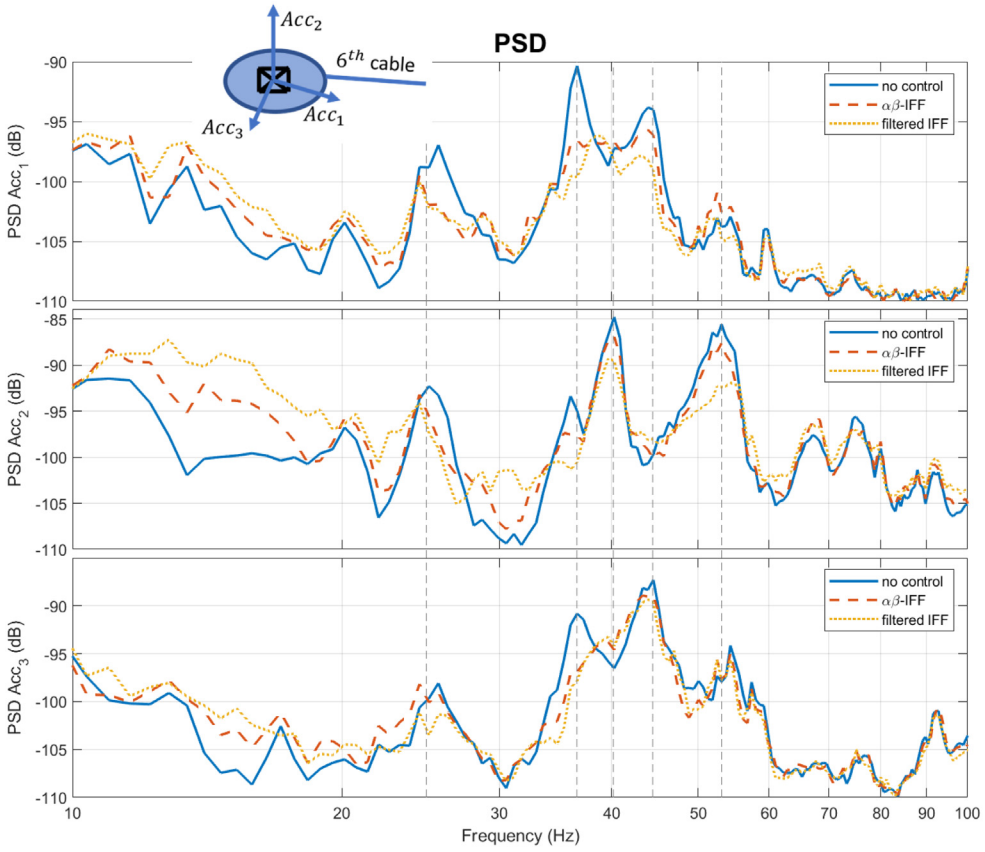

Fig. 7. PSD of acceleration signals without control (blue), with $\alpha\beta$-IFF (red) and with the filtered IFF (yellow).

Table 1. Vibration reductions obtained for the 3 main modes and for each control law.

A_{cc_1}	Frequencies (Hz)	25	36	44
	$\alpha\beta$ − IFF (dB)	2.5	6.2	1.9
	Filtered IFF (dB)	3.1	5.8	4.1
A_{cc_2}	Frequencies (Hz)	25	40	53
	$\alpha\beta$ − IFF (dB)	0.9	2.1	2.1
	Filtered IFF (dB)	1.8	4.5	6.3
A_{cc_3}	Frequencies (Hz)	36	44	54
	$\alpha\beta$ − IFF (dB)	6.1	1.7	0.8
	Filtered IFF (dB)	7	2	1.5

5.4 Limitations of the actuators

Figure 9 presents actuator signal V_{a1} for the three controllers. The operating range of the actuators is limited by the values −16 and 136 V. Only the filtered IFF controller reaches these limits. As stated in Section 3, not all modes are at their maximum damping with $g = 500$. However, the actuator of the active cable no1 is already saturated with $g_1^1 = 400$. With a higher gain, it is theoretically possible to achieve better results with the filtered IFF controller. Therefore, one possibility to increase performance is to use more powerful actuators.

The $\alpha\beta$-IFF signal requires a peak-to-peak amplitude of less than 40 V for good performance with, for example, a 6 dB decrease on the 36 Hz mode on accelerations 1 and 3.

Figure 10 shows the PSD of actuator signal V_{a1} for the three controllers. It can be seen that the power required for $\alpha\beta$-IFF is lower, with an RMS value of 0.0108. This controller can be a good solution if the available power is low. For the filtered IFF controller, the RMS value is 0.0184 and with the PIFF controller, slightly less power is required, with an RMS value of 0.0155, which can limit saturation in some cases.

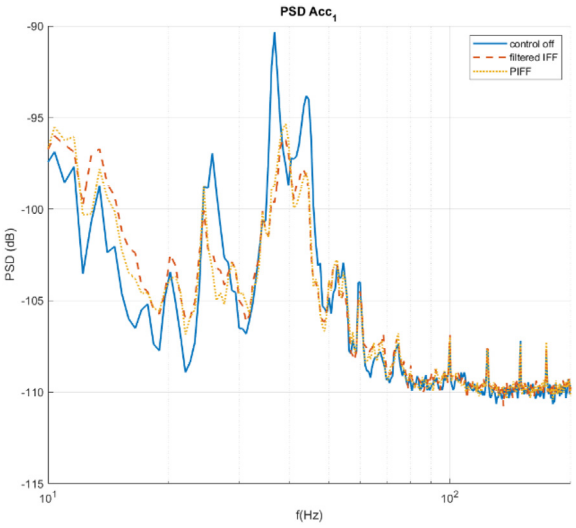

Fig. 8. PSD of acceleration signal A_{cc1} without control (blue), with filtered IFF (red) and with PIFF (yellow).

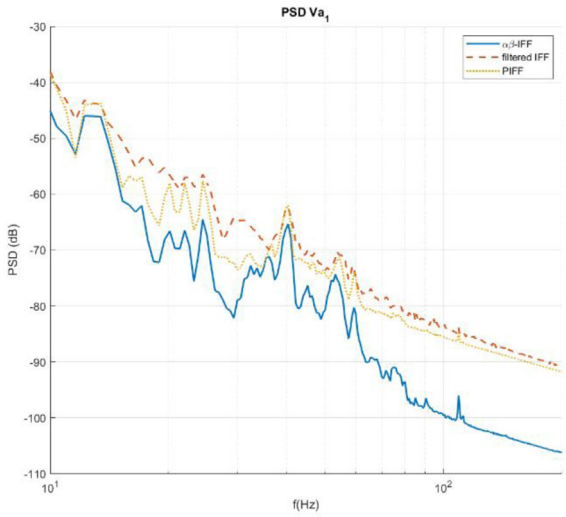

Fig. 10. PSD of actuator signal V_{a1} with $\alpha\beta$-IFF (blue), with filtered IFF (red) and with PIFF (yellow).

Table 2. RMS values for all control laws and accelerations signals.

RMS	A_{cc_1}	A_{cc_2}	A_{cc_3}	$\|A_{cc}\|$
Control off	1.07e-4	2.11e-4	1.49e-4	1.64e-4
$\alpha\beta$ − IFF	9.78e-5	2.01e-4	1.42e-4	1.53e-4
Filtered IFF	9.42e-5	1.98e-4	1.37e-4	1.48e-4
PIFF	9.36e-5	1.76e-4	1.35e-4	1.37e-4

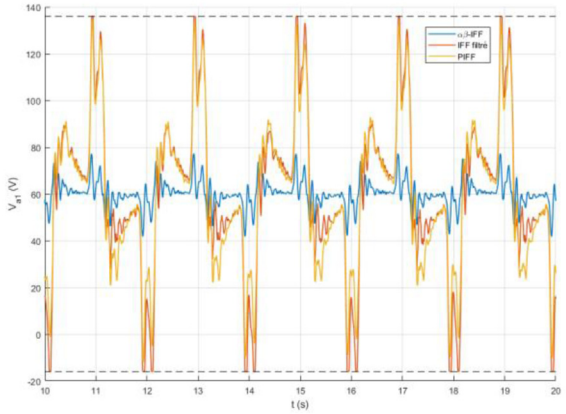

Fig. 9. Actuator signal V_{a1} with $\alpha\beta$-IFF (blue), with filtered IFF (red) and with PIFF (yellow).

6 Conclusion

In this study, two active rods were integrated in a CDPR to reduce the vibrations caused by the effector displacement. Three control laws were presented: αβ-IFF, filtered IFF and PIFF. The dynamic model of the CDPR was used to plot the root locus for the three laws, show their stability and compare their control. In terms of damping, the best controller was the PIFF, obtained and set using the CDPR model.

An experimental set-up was built to validate these results. The prototype consisted of a CDPR with eight cables, two of which were equipped with active rods. An electric motor was used to move the effector and perturb the system. A parametric optimisation was carried out and showed that the PIFF provided the best levels of vibration reduction. Depending on the application, the $\alpha\beta$ − IFF may be a good compromise as it requires a smaller actuation range. The performances were measured with a sensor external to the control loop of the active system, which shows the effectiveness of the vibration control. It was shown that two active rods were sufficient to reduce the vibration amplitudes of the six main robot modes. However, in this setup, the performance was limited by actuator saturation and the fact that only one direction of movement was possible. The generalisation of the results has only been proven by simulation in [24]. But it still allows, without optimization, a proof of concept for the proposed innovation.

In future studies, the active rods will be integrated in a robot driven by 8 motors with more complex trajectories. An avenue for improvement is to test more powerful actuators to achieve higher damping.

Funding

The authors disclose receipt of the following financial support for the research, authorship, and/or publication of this article: the funds provided by the Région Auvergne-Rhônes-Alpes (CabFab project) are gratefully acknowledged.

Conflicts of interest

The authors declare no conflict of interest.

Data availability statement

This article has no associated data generated and/or analysed.

Author contribution statement

Conceptualization, F.L., D.R. and S.C.; Methodology, F.L., D.R. and S.C.; Experimental validation, F.L. and R.D.; Resources, D. R. and S.C.; Writing – Original Draft Preparation, F.L.; Writing – Review & Editing, F.L., D.R. and S.C.

References

[1] S. Bouchard, Géométrie des Robots Parallèles Entraînés par des Câbles (2008), p. 248

[2] C. Gosselin, S. Bouchard, A gravity-powered mechanism for extending the workspace of a cable-driven parallel mechanism: application to the appearance modelling of objects, Int. J. Autom. Technol. **4**, 372–379 (2010)

[3] R. Chellal, L. Cuvillon, E. Laroche, Model identification and vision-based H_∞ position control of 6-DoF cable-driven parallel robots, Int. J. Control **90**, 684–701 (2017)

[4] R. Bostelman, J. Albus, N. Dagalakis, A. Jacoff, J. Gross, Applications of the NIST Robocrane, Robot. Manufactur. **5** (1994)

[5] E. Barnett, C. Gosselin, Large-scale 3D printing with a cable-suspended robot, Additive Manufactur. **7**, 27–44 (2015)

[6] S. Kawamura, H. Kino, C. Won, High-speed manipulation by using parallel wire-driven robots, Robotica **18**, 13–21 (2000)

[7] S. Kawamura, W. Choe, S. Tanaka, H. Kino, Development of an ultrahigh speed robot FALCON using wire drive systems, J. Robotics Soc. Jpn. (1997)

[8] X. Weber, L. Cuvillon, J. Gangloff, Active vibration canceling of a cable-driven parallel robot in modal space, in *2015 IEEE International Conference on Robotics and Automation (ICRA)* (2015), p. 1599–1604

[9] S. Baklouti, E. Courteille, P. Lemoine, S. Caro, Input-Shaping for Feed-Forward Control of Cable-Driven Parallel Robots, arXiv:2010.11676 [physics] (2020). doi: 10.1115/1.4048354

[10] B. Zi, B.Y. Duan, J.L. Du, H. Bao, Dynamic modeling and active control of a cable-suspended parallel robot, Mechatronics **18**, 1–12 (2008)

[11] X. Weber, L. Cuvillon, J. Gangloff, Active vibration canceling of a cable-driven parallel robot using reaction wheels, in *2014 IEEE/RSJ International Conference on Intelligent Robots and Systems* (2014), p. 1724–1729

[12] M. Lesellier, L. Cuvillon, J. Gangloff, M. Gouttefarde, An active stabilizer for cable-driven parallel robot vibration damping, in *2018 IEEE/RSJ International Conference on Intelligent Robots and Systems (IROS)* (2018), p. 5063–5070

[13] M. Rushton, Vibration Control in Cable Robots Using a Multi-Axis Reaction System (2016). Available from: https://uwspace.uwaterloo.ca/handle/10012/10945

[14] M. Rushton, A. Khajepour, Transverse vibration control in planar cable-driven robotic manipulators, in *Cable-Driven Parallel Robots*, edited by C. Gosselin, P. Cardou, T. Bruckmann, A. Pott (Springer International Publishing, Cham, 2018), pp. 243–253

[15] F. Bossens, Amortissement actif des structures câblées: de la théorie à l'implémentation, Université Libre de Bruxelles, Brussels, Belgium (2001)

[16] Y. Achkire, A. Preumont, Active tendon control of cable-stayed bridges, Earthquake Eng. Struct. Dyn. **25**, 585–597 (1996)

[17] A. Preumont, M. Voltan, A. Sangiovanni, B. Mokrani, D. Alaluf, Active tendon control of suspension bridges, Smart Struct. Syst. **18**, 31–52 (2016)

[18] D. Mohammadshahi, Dynamics and Control of Cables in Cable-Actuated Systems (2013), p. 92

[19] M. Verma et al., Dynamic stabilization of thin aperture light collector space telescope using active rods, JATIS **6**, 014002 (2020)

[20] A. Preumont, A. François, F. Bossens, A. Abu-Hanieh, Force feedback versus acceleration feedback in active vibration isolation, J. Sound Vibrat. **257**, 605–613 (2002)

[21] A. Preumont, Vibration Control of Active Structures: An Introduction (Springer, 2018)

[22] B. de Marneffe, Active and passive vibration isolation and damping via shunted transducers, Faculté des Sciences Appliquées, Université Libre de Bruxelles, 2007. Disponible sur: https://scmero.ulb.ac.be/Publications/Thesis/de_Marneffe07.pdf

[23] S. Chesné, A. Milhomem, C. Collette, Enhanced damping of flexible structures using force feedback, J. Guidance Control Dyn. **39**, 1654–1658 (2016)

[24] F. Lacaze, A. Paknejad, D. Remond, S. Chesne, Improved integral force feedback controllers for lightweight flexible structures, J. Vibr. Control 1077546320974549 (2020)

[25] D. Gueners, H. Chanal, B.C. Bouzgarrou, Stiffness optimization of a cable driven parallel robot for additive manufacturing, in *2020 IEEE International Conference on Robotics and Automation (ICRA)* (2020), pp. 843–849

[26] X. Diao, O. Ma, Vibration analysis of cable-driven parallel manipulators, Multibody Syst. Dyn. **21**, 347–360 (2009)

[27] A. Glumineau, J. de León Morales, Robust Synchronous Motor Controls Designs (PMSM and IPMSM), in *Sensorless AC Electric Motor Control: Robust Advanced Design Techniques and Applications*, edited by A. Glumineau, J. de León Morales (Springer International Publishing, Cham, 2015), pp. 121–142

[28] R.H. Park, Two-reaction theory of synchronous machines generalized method of analysis-part I, Trans. Am. Inst. Electr. Eng. **48**, 716–727 (1929)

[29] P. Welch, The use of fast Fourier transform for the estimation of power spectra: A method based on time averaging over short, modified periodograms, IEEE Trans. Audio Electroacoust. **15**, 70–73 (1967)

Cite this article as: F. Lacaze, R. Delpoux, D. Remond, S. Chesne, Active vibration control of a cable-driven parallel robot using active rods, Mechanics & Industry **25**, 27 (2024)